



# Photocatalytic Performance of Highly Active Brookite in the Degradation of Hazardous Organic Compounds Compared to Anatase and Rutile



Huyen Thi Thuong Tran<sup>a,c</sup>, Hendrik Kosslick<sup>a,b,\*</sup>, Muhammad Farooq Ibad<sup>a,b</sup>, Christine Fischer<sup>b</sup>, Ursula Bentrup<sup>b</sup>, Thanh Huyen Vuong<sup>b</sup>, Liem Quang Nguyen<sup>c</sup>, Axel Schulz<sup>a,b,\*</sup>

<sup>a</sup> University of Rostock, Institute of Chemistry, Department of Inorganic Chemistry, Albert-Einstein-Str. 3a, Rostock, Germany

<sup>b</sup> Leibniz Institute of Catalysis e.V. (LIKAT), Albert-Einstein-Str. 29a, Rostock, Germany

<sup>c</sup> Institute of Materials Science (IMS), Vietnam Academy of Science and Technology (VAST), 18 Hoang Quoc Viet, Cau Giay, Hanoi, Viet Nam

## ARTICLE INFO

### Article history:

Received 3 May 2016

Received in revised form 1 July 2016

Accepted 14 July 2016

Available online 15 July 2016

### Keywords:

Anatase

Brookite

Rutile

Pharmaceutical

Photocatalytic degradation

## ABSTRACT

The photocatalytic activity of brookite was studied and compared with anatase, rutile, and commercial titania P25 (Degussa). Brookite exhibited relatively high activity in the degradation of different hazardous compounds under sunlight equivalent conditions. Brookite and other titania polymorphs anatase and rutile were hydrothermally synthesized under the similar reaction conditions starting with the same amorphous titania precursor. The highly crystalline titania polymorphs were characterized by XRD, SEM, TG-DSC, Raman- and diffuse reflectance UV-vis spectroscopy. Brookite (B) and anatase (A) crystallized in form of agglomerated spherical-shaped nanoparticles of ca. 10 nm in size. Rutile (R) formed up to 500 nm large rod-like nanocrystals. The band gaps of the titania polymorphs were about 3.25–3.34 eV. The aromatic ring opening in different hazardous compounds was monitored by UV-vis absorption spectroscopy and the mineralization was determined by total organic carbon (TOC) measurements. Additionally, the formation of intermediates was studied by electrospray ionization time-of-flight mass spectra (ESI-TOF-MS). The recalcitrance of organic compounds against the photocatalytic degradation increases in the following order: cinnamic acid < ibuprofen < phenol. The general order of photocatalytic activity was B ≈ A > R.

© 2016 Elsevier B.V. All rights reserved.

## 1. Introduction

To date the common contaminants such as pharmaceutical and phenolic compounds have attracted considerable attention. Most of these contaminants come either from domestic wastewater or from hospital or industrial effluents and end up back in the environment. Around 90% of wastewater produced globally remains untreated causing the water pollution [1]. Much attention is focused on pharmaceuticals due to the multitude of pharmaceuticals applied in medicine [2,3]. They are partially metabolised by humans or animals and are exposed to municipal wastewater along with excreta [2–4]. Besides, these contaminants vary not only in composition

but also in quantity depending on the raw materials as water and the processes involved in the pharmaceutical manufacturing [1]. Removal efficiencies of pharmaceuticals were reported from 10 to 90% in German rivers and streams [5], ≥50% in French drinking water [6]. In another report, ca. 80% of pharmaceuticals and personal care products was removed in USA [7].

Studies on the occurrence of pharmaceutical compounds showed that ibuprofen (IBP), a non-steroidal anti-inflammatory drug (NSAID), is one of the most consumed pharmaceuticals [4,5,7]. It is widely used to reduce fever and treat pain or inflammation caused by many conditions such as headache, toothache, or back pain [8–10]. Due to the high application level and the fact that this pharmaceutical can be purchased without prescription, there is a wide range of ibuprofen concentrations from 65 to 7100 ng/L in wastewater treatment plants and raw wastewater effluents, and up to 360 ng/L in freshwater [8,11]. Another organic compound to consider is cinnamic acid (CA), which exists as *cis*- and *trans*-isomer, but the *trans* form is more common. It is widely used in food

\* Corresponding authors at: University of Rostock, Institute of Chemistry, Department of Inorganic Chemistry, Albert-Einstein-Str. 3a, Rostock, Germany.

E-mail addresses: [hendrik.kosslick@uni-rostock.de](mailto:hendrik.kosslick@uni-rostock.de) (H. Kosslick), [axel.schulz@uni-rostock.de](mailto:axel.schulz@uni-rostock.de) (A. Schulz).

industry (as a flavouring agent in baked goods, sweets, ice cream, beverages, and chewing gum) [12], in cosmetics (perfumes, decorative cosmetics, fine fragrances, shampoos, toilet soaps) as well as in non-cosmetics (household cleaners and detergents) [13]. Additionally, cinnamic acid is used as pharmaceuticals for preventing high blood pressure or possessing antitumor activity [14]. In a recent review, cinnamic acid and its derivatives have been received much attention in medicinal research as synthetic antitumor agents [15]. It also is the widespread released pollutant in olive oil production [16].

Beside the pharmaceutical compounds, the presence of phenol and its derivatives in wastewater of many industries including resins, petrochemical, paint, textile, oil refineries, food, photographic chemicals, antioxidants and flavouring agents is another problem attracting global concern [17,18]. Phenol is typical of phenolic compound and it is considered to be an intermediate product in the oxidation reactions of higher molecular weight compounds [19]. European Union (EU) has classified several phenols as priority contaminants and the 80/778/EC directive states a maximum concentration of 0.5 µg/L for total phenols in drinking water. Individual concentration should be under 0.1 µg/L [17]. Due to their toxic and endocrine disrupting properties, many studies have focused on removing phenolic compounds from drinking water and wastewater as well [19–25].

Considering the widespread occurrence, the hazardous nature and the harmful effects, it is essential to remove pharmaceutical and phenolic compounds in water. However, incomplete removal of pollutants has been reported by using conventional processes as biological process (biodegradation), physical process (e.g., adsorption), or chemical process (e.g., ozonation). By biological treatment, ca. 70% of ibuprofen was removed, the latter are toxic and stable by-products as carboxylated and/or hydroxylated IBP [2,26,27]. Among advanced oxidation processes (AOPs), heterogeneous photocatalysis has been commonly used as an alternative to decompose organic contaminants in water [26,28–34]. This process is non-selective and could achieve rapid and complete degradation because of the attack of oxidative species [35–37]. The valence band holes ( $\text{h}^+$ ) have high oxidation potential of up to +3.5 V vs. NHE (normal hydrogen electrode) depending on the semiconductor catalysts (e.g.,  $\text{TiO}_2$ ,  $\text{ZnO}$ ,  $\text{ZrO}_2$ , ...) [38]. However, the hydroxyl ( $\cdot\text{OH}$ ) radicals (redox potential +2.8 V vs. NHE) have received most attention in the photocatalytic degradation of organic pollutants [29,30,39–41]. The other advantage of photocatalysis is the ability of using solar light as ultraviolet (UV) or visible light source and oxygen from the air and/or water as oxidizing agent [42–44].

Photocatalysis using a semiconductor catalyst as  $\text{TiO}_2$  is an environmentally-friendly approach with the advantages such as: (i) low cost, (ii) chemical stability, (iii) high oxidizing ability, (iv) safety, and (v) reusability [28,29,31,38,45]. According to the previous reports, the photocatalytic activity of  $\text{TiO}_2$  is dependent on the surface and structural properties such as surface area [46,47], crystal composition [48], particle size distribution, porosity, band gap and surface hydroxyl density [49–51]. In general, the smaller the particle size, the larger the surface area [30]. Thus, it can increase the number of active sites and adsorb more target molecules (higher organic loading) leading to enhance the photocatalytic efficiency. At nanoscale range, physical and chemical properties of semiconductor catalysts can be modified and optimized by changing the size. Nanoparticles usually not only offer desired crystalline structure but also come with a large surface area (high adsorption capacity) [35,52]. Most studies on the photocatalytic performance were conducted with either anatase [53–58] or rutile [51,59,60]. In contrast, brookite is much less studied but is a promising catalyst for photocatalytic applications [58,61]. Brookite often co-crystallizes with anatase and/or rutile which requires additional separation procedures [61–63].

As a result, many previous papers deal with biphasic, triphasic mixtures/composites of brookite/rutile [64–70], brookite/anatase [70–76], or anatase/brookite/rutile [56,70,72,73,77,78].

This study presents a comprehensive comparison of the photocatalytic performance of brookite, anatase, and rutile in the degradation of different recalcitrant molecules, the pharmaceutical ibuprofen (IBP), the recalcitrant phenol (Ph), and the more reactive cinnamic acid (CA). The photocatalytic experiments were conducted under reliable conditions as (i) low power sunlight equivalent irradiation with an UV-vis solarium lamp, (ii) low catalyst concentration, and (iii) high organic loading. The degradation is studied by UV-vis absorption spectroscopy (destruction of the aromatic ring). The mineralization, i.e., the complete abatement of the organic pollutants to carbon dioxide and water, was followed by TOC measurements. Finally, the results are compared with the commercial photocatalyst titania P25.

## 2. Experimental

### 2.1. Materials

All of the chemicals were of analytical grade and used without further purification: titanium(IV) *i*-propoxide (TTIP, Merck, 98%), hydrochloric acid (HCl, Chemsolute, 35–38%), glacial acetic acid ( $\text{CH}_3\text{COOH}$ , Chemsolute, 99.7%), isopropanol ( $\text{C}_3\text{H}_8\text{O}$ , Sigma-Aldrich, >99%), titania P25 ( $\text{TiO}_2$ , Degussa, 99.5%), ibuprofen sodium salt ( $\text{C}_{13}\text{H}_{17}\text{O}_2\text{Na}$ , Sigma-Aldrich, 98%), cinnamic acid ( $\text{C}_9\text{H}_8\text{O}_2$ , Reachim, 99%), phenol ( $\text{C}_6\text{H}_6\text{O}$ , Sigma-Aldrich, 99%).

### 2.2. Synthesis of photocatalysts

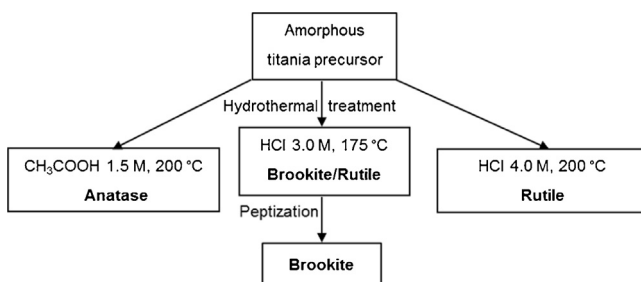
Three titania polymorphs brookite, anatase, and rutile were prepared according to a previous report which was optimized [63]. There are two stages including the sol-gel synthesis and the hydrothermal treatment of amorphous titania. The detailed synthesis procedure is as follows:

#### 2.2.1. Sol-gel synthesis of amorphous titania precursor

Amorphous titania was synthesized by hydrolysis and condensation of titanium(IV) isopropoxide (TTIP) as titanium precursor. First, 20 mL of TTIP was dissolved in 105 mL of isopropanol. Hydrolysis was performed by adding the mixed solution (105 mL of isopropanol and 1 mL of water) prepared at room temperature (RT) slowly into the above solution that was maintained at 0 °C in an ice bath. The white titanium hydroxide precipitates were formed after 4 h of the addition of water. Then, the mixed solution was continued under a vigorous stirring at RT for 24 h. Thereafter, the white precipitates were separated from the reaction solution by centrifugation (9000 rpm, 10 min). The remaining solution was again diluted with 1 L of water, followed by stirring at RT for 24 h, and finally separated by centrifugation. The final obtained precipitates were washed with water and ethanol and then dried in vacuum at 60 °C to get white powder.

#### 2.2.2. Hydrothermal treatment of amorphous titania precursor

1.0 g of the obtained amorphous titania powder was given into the 120 mL Teflon cup and then a concentrated aqueous acidic solution was added to achieve a 0.3 M solution. The obtained suspension was stirred at RT for 30 min. Subsequently, the Teflon cup was transferred into a stainless steel-lined autoclave, which was placed into an oven and heated at elevated temperature for 7 h. The experiments were conducted with different temperatures, acid types, and acid concentrations in order to obtain the desired titania phases (Scheme 1). After hydrothermal treatment, the autoclave was cooled to RT naturally, and the obtained precipitates were decanted, then washed thoroughly with distilled water and



**Scheme 1.** Synthesis of phase-pure titania polymorphs.

ethanol, and finally dried at 60 °C overnight in oven. All products were grinded in a porcelain mortar with a pestle to get fine powders.

### 2.3. Characterization

The morphology of TiO<sub>2</sub> samples was studied by scanning electron microscopy (SEM) using an S4800 field emission scanning electron microscope (FE-SEM, Hitachi, Japan) at an accelerating voltage of 5 kV. The X-ray diffraction (XRD) patterns were recorded on a STADI-P X-ray diffractometer (STOE) using monochromatic CuK $\alpha$  radiation ( $\lambda = 1.5406 \text{ \AA}$ ). The crystallite sizes of samples were estimated from the widths XRD diffraction reflection using the Scherrer equation [79]:  $D = k\cdot\lambda/\beta\cdot\cos\theta$ , where D is the average crystallite size, k is the Scherrer constant (0.9),  $\lambda$  is X-ray wavelength, and  $\beta$  is the width at half height of the reflection at the corresponding diffraction angle  $\theta$ . Raman spectra were recorded on a LabRAM HR 800 Raman microscope system (Horiba Jobin YVON) equipped with a high stability BX40 microscope (focus 1  $\mu\text{m}$ ). A blue laser (473 nm, 20 mW air-cooled solid-state laser) was used for excitation. Diffuse reflectance UV-vis (DR-UV-vis) spectra of titania polymorphs were measured at RT using a Cary 5000 spectrometer (Varian) equipped with a diffuse reflectance accessory (praying mantis, Harrick). The spectra were collected

in the range of 200–800 nm using BaSO<sub>4</sub> as reference material and converted into the Kubelka-Munk function F(R). By plotting  $(F(R)\cdot h\nu)^{1/2}$  vs.  $(h\nu)$  and  $(F(R)\cdot h\nu)^2$  vs.  $(h\nu)$  for indirect and direct band gaps, respectively, Tauc plots were obtained.  $h\nu$  is the photon energy and F(R) is the absorption coefficient. The band gaps ( $E_g$ ) were determined by extrapolating the straight line of the plots at the point  $(F(R)\cdot h\nu)^{1/2} = 0$  and  $(F(R)\cdot h\nu)^2 = 0$  on  $h\nu$ -axis [63,66,80]. N<sub>2</sub> adsorption-desorption isotherms were measured at 77 K on a Thermo Sorptomatic 1990 instrument. The specific surface area was determined by the BET (Brunauer-Emmett-Teller) method using the relative pressure range of 0.05–0.35. The porosity (pore size and specific pore volume) of samples was determined from the desorption branch of the isotherm in the relative pressure range of 0.3–0.99 using the BJH (Barrett-Joyner-Halenda) method. Thermal analysis was performed on a Setaram TGA Labsys 1600 DSC under Argon gas at a heating rate of 10 K/min. The weight loss was evaluated on the derivation of the thermogravimetry (TG) curve. The 0.1 cm<sup>3</sup> alumina (Al<sub>2</sub>O<sub>3</sub>) crucibles were used.

The UV-vis absorption spectra of organic aqueous solution were measured using a Lambda 19 UV-vis spectrometer (Perkin Elmer). The photocatalytic degradation was determined by the change in the intensity of absorption band of treated organic aqueous solution. The formation of reaction intermediates/by-products was studied by electrospray ionization time-of-flight mass spectrometry (ESI-TOF-MS) using an electrospray ionization mass spectrometer HPLC System 1200/ESI-TOF-MS 6210 (Agilent). The measurements were carried out in negative ionization mode. An aqueous solution containing 10 vol.% of methanol (HPLC, gradient grade, ≥99.8%) and 0.1 vol.% of formic acid (HCOOH) was used as mobile phase. The flow rate was 1.0 mL/min. The mass-to-charge ( $m/z$ ) was scanned in the mass range of  $m/z$  0–1000. The degree of mineralization, the change in the carbon content present in reaction solution was measured by a TOC analyser (TOC-L CSH/CSN, Shimadzu).

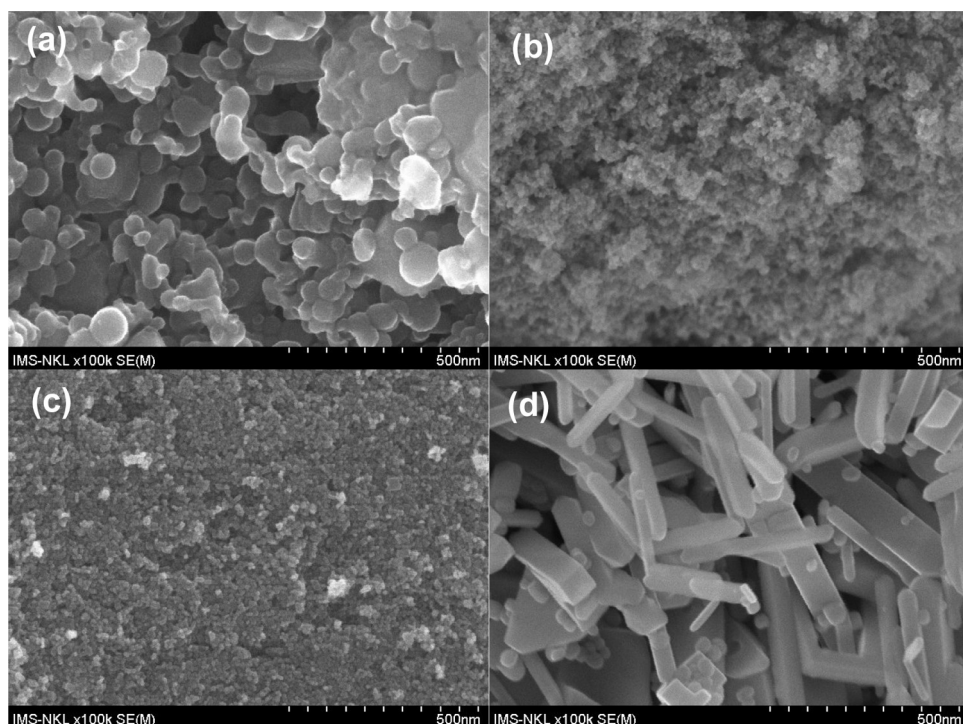


**Fig. 1.** SEM images of (a) amorphous titania, (b) anatase, (c) brookite, and (d) rutile.

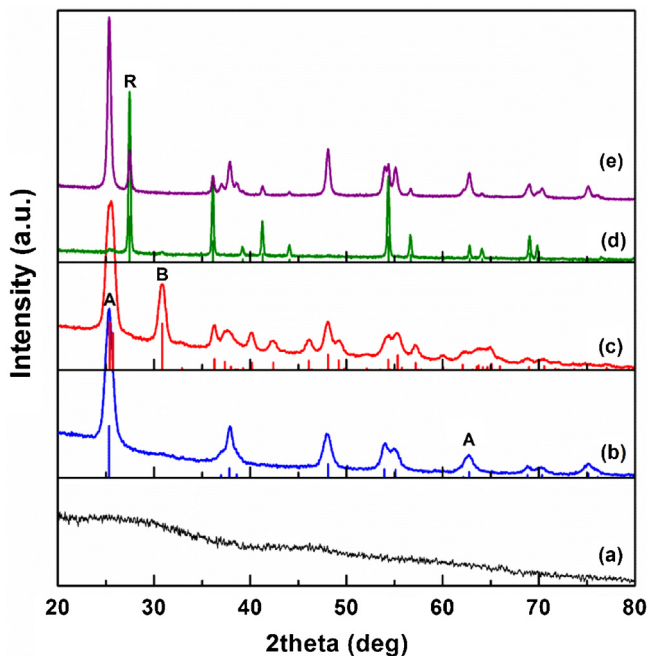


**Fig. 2.** XRD patterns of (a) amorphous titania, (b) anatase, (c) brookite, (d) rutile, and (e) titania P25. Pattern (b), (c) and (d) include the calculated diffraction lines from the corresponding JCPDS databases (b) 96-900-9087, (c) 96-900-9088, and (d) 96-900-9084. A, B, and R denote anatase, brookite, and rutile phase, respectively.

#### 2.4. Photocatalysis

The photocatalytic experiments were carried out in a batch reactor using ibuprofen (IBP), cinnamic acid (CA), and phenol (Ph) as model organic pollutants. The UV-vis solarium lamp (60 W, Philips) was used as light source, which simulated the UV part of sunlight (by light energy distribution and intensity) in the range of *ca.* 370–400 nm. The distance from the applied lamps to the surface of pollutant solution was 15 cm. 10 mg of photocatalyst was added into 250 mL of 10 ppm organic aqueous solution to form suspension. Before illumination, the suspension was stirred for 30 min in dark to obtain adsorption equilibrium. After a certain period of time, 5 mL aliquot was taken from the suspension by a syringe and separated from the photocatalyst by a 0.45 µm PTFE filter. The photocatalytic abatement of IBP, CA, Ph was determined by the change in the intensity of the absorption band at 221, 273, 270 nm, respectively.

### 3. Results and discussion

#### 3.1. Hydrothermal synthesis

Highly crystalline TiO<sub>2</sub> samples of brookite, anatase and rutile were prepared by hydrothermal synthesis under selected acidic conditions using an amorphous titania as starting material (**Scheme 1**). The latter was obtained by a controlled hydrolysis of TTIP in isopropanol with addition of a small amount of water. The subsequent condensation led to the formation of a Ti-O-Ti network (gel). The drying procedure resulted in an amorphous titania powder which was used without calcination for the hydrothermal synthesis of the different titania polymorphs. More importantly, the advantage of this synthetic approach is that all titania polymorphs were obtained under similar reaction conditions (amorphous titania precursor, acidic media, and reaction time). Thus, the impact of synthesis procedure on the photocatalytic activity of titania polymorphs was diminished. Whereas phase-pure anatase and rutile can be directly synthesized, brookite is always formed in the mix-

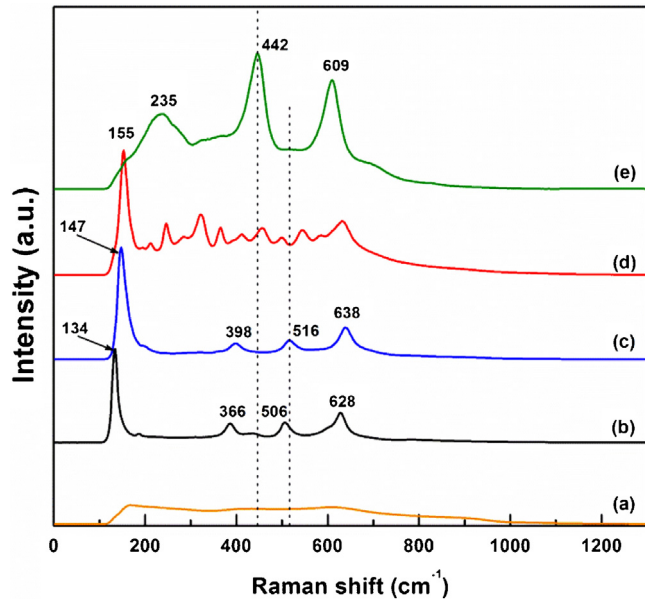


**Fig. 3.** Raman spectra of (a) amorphous titania, (b) titania P25, and the synthesized titania polymorphs (c) anatase, (d) brookite, and (e) rutile.

ture with rutile. Namely, acetic acid was used for the synthesis of phase-pure anatase by hydrothermal treatment at 200 °C. With the same reaction temperature, the use of 4.0 M HCl yielded rutile. At lower HCl concentration (3.0 M) and lower treatment temperature (175 °C), a mixture of brookite and rutile were formed. Phase-pure brookite was separated effectively from the mixture by peptization in water.

The morphology (shape and size) of synthesized titania polymorphs was studied by SEM. **Fig. 1** shows SEM images of amorphous titania precursor and the hydrothermal synthesis products anatase, brookite, and rutile. The amorphous titania particles are spherical in shape and *ca.* 50–100 nm in size (**Fig. 1a**). Both anatase and brookite form aggregated round-shaped nanoparticles of *ca.* 10 nm size (**Fig. 1b** and **c**). These crystal sizes are in agreement with XRD results (**Fig. 2**), which show crystallite sizes of *ca.* 10 nm for anatase and *ca.* 12 nm for brookite determined by the Scherrer equation. In contrast, rutile forms large rod-shaped nanocrystals (**Fig. 1d**) which are up to *ca.* 50–100 nm in width and *ca.* 300–500 nm in length. Besides, some spherical nanoparticles are observed with particle size of *ca.* 50 nm which belong likely to non-reacted amorphous titania.

#### 3.2. Characterization

**Fig. 2** shows the XRD patterns of the three titania polymorphs obtained by hydrothermal treatment. These patterns are compared to those of the amorphous titania precursor and the titania P25 (Degussa). The titania precursor is amorphous and shows no diffraction pattern (**Fig. 2a**). The directly prepared anatase and rutile samples show structural characteristic and well resolved XRD patterns (**Fig. 2b** and **d**). The intensities and diffraction angles of reflections are consistent with the theoretical diffraction patterns from the JCPDS databases. No additional reflections related to impurities could be detected. The XRD patterns of anatase and brookite (**Fig. 2b** and **c**) show comparatively broad reflections which confirm the formation of small crystallites of *ca.* 10 nm size as shown by SEM. In contrast, narrow reflections are observed with rutile (**Fig. 2d**). Rutile forms remarkably larger crystals with crystallite sizes of *ca.* 98 nm. Also the reflections of titania P25 are relatively narrow (**Fig. 2e**) indicating the larger crystallite sizes, *i.e.*, high crystallinity. It has to be noted that titania P25 is industrially

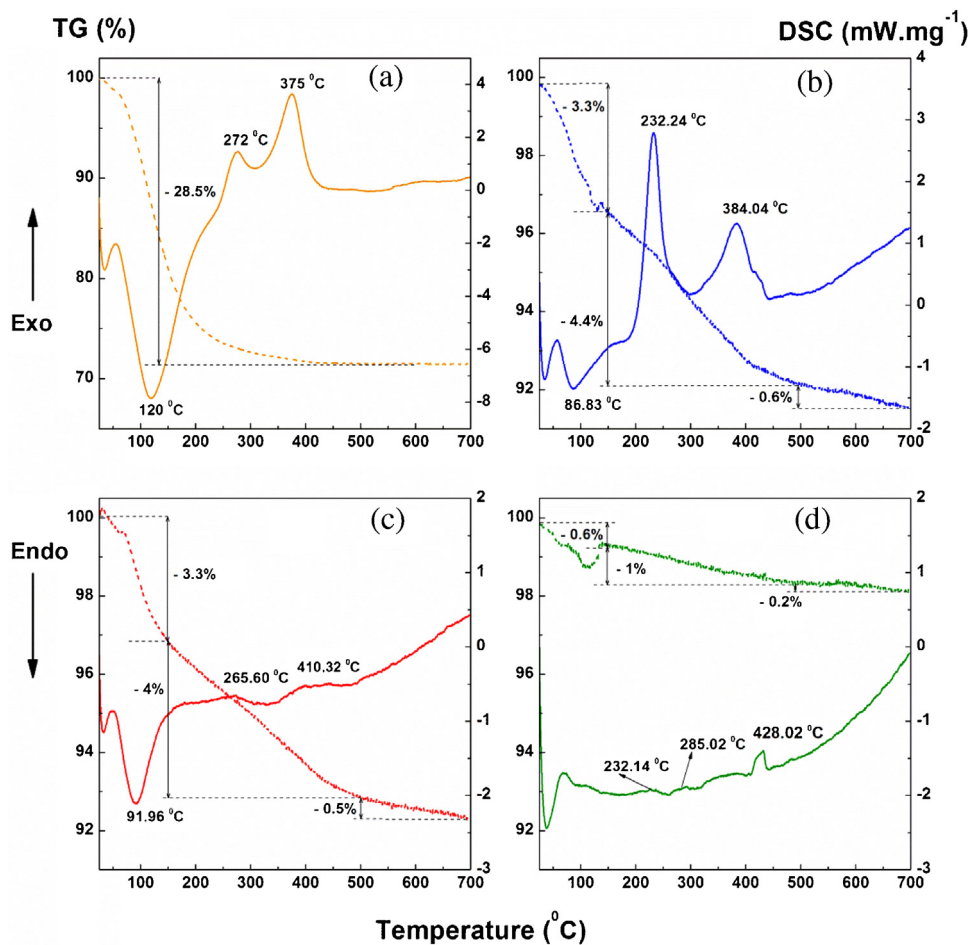


**Fig. 4.** TG-DSC curves of (a) amorphous titania, (b) anatase, (c) brookite, and (d) rutile.

synthesized by high temperature pyrolysis of titanium(IV) chloride ( $\text{TiCl}_4$ ) [73] yielding a high crystalline anatase/rutile mixture.

Complementary, Raman spectroscopy was used to investigate  $\text{TiO}_2$  samples, because they show structure dependent characteristic Raman bands which allow identifying the crystal phase and composition of mixtures (Fig. 3). The Raman spectrum of titania P25 (Degussa) containing Raman bands of anatase and rutile was studied for comparison (Fig. 3b). In the spectrum of brookite (Fig. 3d), a strong band at  $155\text{ cm}^{-1}$  corresponding to  $\text{A}_{1g}$  mode is observed. Besides, the weaker Raman bands are observed in the range of  $200\text{--}700\text{ cm}^{-1}$ . They are assigned to the vibrational modes  $\text{A}_{1g}$  ( $249, 411, 545$  and  $637\text{ cm}^{-1}$ ),  $\text{B}_{1g}$  ( $213\text{ cm}^{-1}$ ),  $\text{B}_{3g}$  ( $324$  and  $501\text{ cm}^{-1}$ ),  $\text{B}_{2g}$  ( $366, 460$  and  $584\text{ cm}^{-1}$ ), respectively [81–83]. More importantly, the formation of phase-pure brookite is confirmed by the absence of the characteristic Raman bands of anatase at  $516\text{ cm}^{-1}$  [61,82] and of rutile at  $442\text{ cm}^{-1}$  [57]. In the spectrum of anatase (Fig. 3c), four Raman bands at  $147, 398, 516$ , and  $638\text{ cm}^{-1}$  are clearly observed, which are assigned to the  $\text{E}_g, \text{B}_{1g}, \text{A}_{1g}$ , and  $\text{E}_g$  modes, respectively [71,82,84]. Three typical bands appear in the Raman spectrum of rutile (Fig. 3e) at  $245, 442$ , and  $607\text{ cm}^{-1}$ , respectively [85,86]. The Raman spectroscopic investigations confirm that all hydrothermal prepared samples anatase, brookite, and rutile are high crystalline and phase-pure. These results are in agreement with our XRD measurements.

The effect of heat treatment in the  $\text{TiO}_2$  samples was studied by TG-DSC analyses as depicted in Fig. 4. In the DSC curve of the amorphous titania (Fig. 4a), we observe a well resolved endothermic peak at  $120\text{ }^\circ\text{C}$  owing to the release of more strongly adsorbed water. The peak is extended to  $200\text{ }^\circ\text{C}$  indicating that dehydroxylation

happens. This assignment is in line with the marked weight loss of *ca.* 23 wt% in this temperature range. The weight loss is extended with further heating to  $400\text{ }^\circ\text{C}$  but with *ca.* 5 wt% much lower than before. At the same time, two exothermic peaks appear at *ca.* 272 and  $375\text{ }^\circ\text{C}$ . Both findings point to the occurrence of a combined dehydroxylation/condensation (endothermic/exothermic) process in the amorphous titania. With anatase, a total weight loss of *ca.* 8.3 wt% is found by heating to  $700\text{ }^\circ\text{C}$  (Fig. 4b). The TG curve shows three main weight loss steps. The first weight loss of *ca.* 3.3 wt% between RT and  $150\text{ }^\circ\text{C}$  is related to physically adsorbed water. The maximum of the corresponding endothermic peak in the DSC curve is located *ca.* at  $86\text{ }^\circ\text{C}$ . The second weight loss of *ca.* 4.4 wt% is observed in the range between  $150$  and  $500\text{ }^\circ\text{C}$  with an intermediate step at  $270\text{ }^\circ\text{C}$ . This weight loss causes two exothermic DSC peaks at *ca.*  $232$  and  $384\text{ }^\circ\text{C}$ . They are assigned to a combined dehydroxylation/condensation process. A further weight loss beyond  $440\text{ }^\circ\text{C}$  proceeds more slowly and is assigned to the dehydroxylation/condensation of remaining surface hydroxyl groups. Compared to anatase, the TG curve of brookite shows a similar behaviour in the weight loss (Fig. 4c). The first weight loss is similar. The related endothermic DSC peak is somewhat extended to higher temperature ( $92\text{ }^\circ\text{C}$ ) and its intensity increased. This indicates stronger bonding of physisorbed water. The second weight loss is accompanied by two main exothermic DSC peaks of low intensity located at *ca.*  $265$  and  $410\text{ }^\circ\text{C}$ . With rutile, the similar weight loss steps occur with endothermic desorption of water and exothermic dehydroxylation/condensation process at higher temperature (Fig. 4d). The total weight loss (*ca.* 1.8 wt%) is low com-

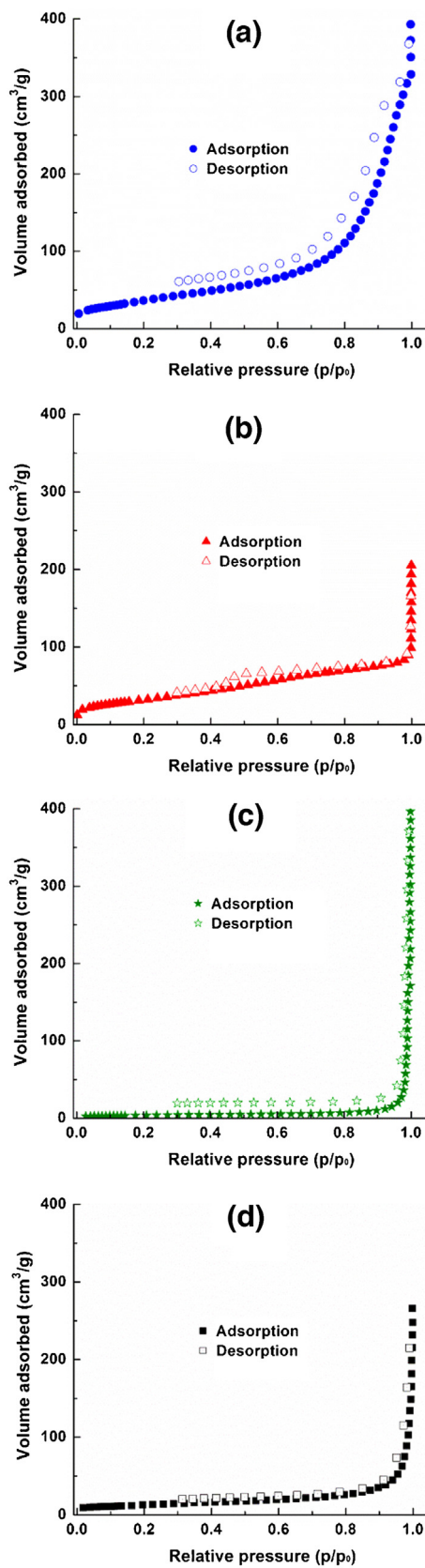


Fig. 5. Nitrogen adsorption-desorption isotherms of (a) anatase, (b) brookite, (c) rutile, (d) titania P25.

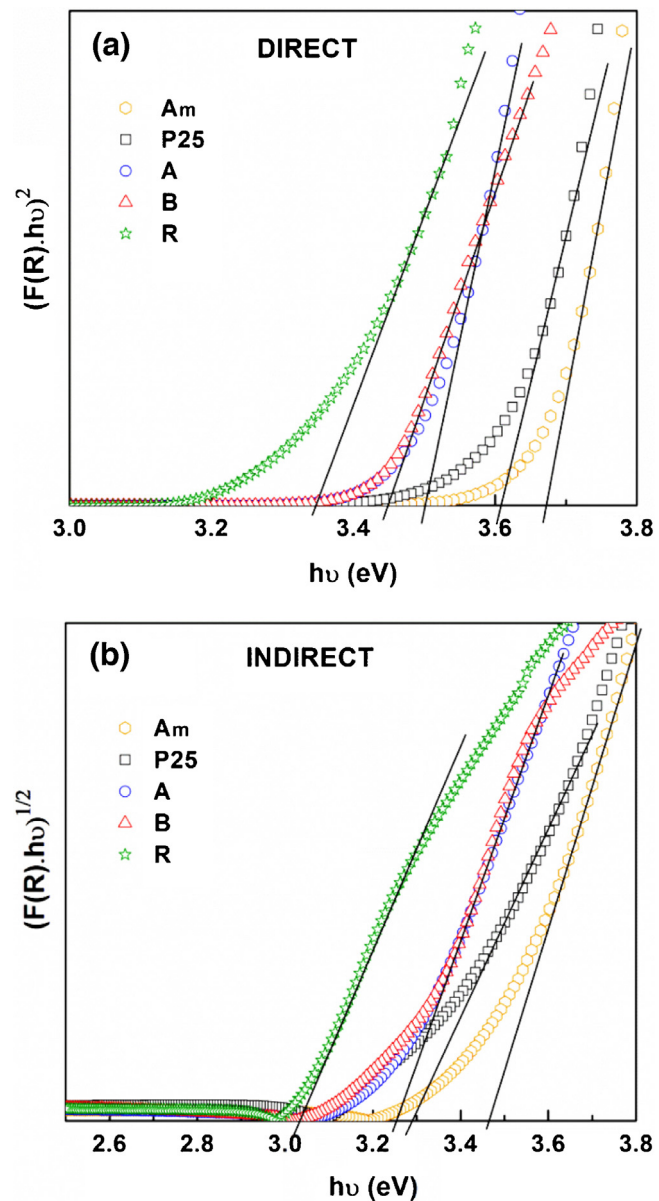


Fig. 6. Tauc plots of amorphous titania (Am), anatase (A), brookite (B), rutile (R), and titania P25 (P25).

pared to brookite or anatase. This is likely due to the large particle size of rutile and, hence, the lower specific surface.

The nitrogen adsorption-desorption isotherms and the corresponding pore size distributions of the synthesized TiO<sub>2</sub> polymorphs and titania P25 (Degussa) are shown in Figs. 5 and S1. The shapes of isotherms belonged to type-V for anatase, rutile, titania P25 and type-IV for brookite. They are characterized by a low nitrogen uptake at the onset, followed by a slight increase of adsorption. This indicated the monolayer coverage of the titania surface until  $p/p_0$  ca. 0.3, followed by multilayer adsorption at higher relative pressure. A steep increase of nitrogen uptake was observed upon  $p/p_0 = 0.8$ . This uptake is assigned to the filling of inter-particle meso- and nanopores of titania agglomerates. The onset of this step varies somewhat for the different titania polymorphs indicating the different particle size and agglomeration. Anatase and brookite show higher specific surface areas of 132 and 116 m<sup>2</sup>/g, respectively, due to the small particle size of ca. 10–12 nm determined by XRD and SEM. In contrast, titania P25 and rutile show distinctly lower specific surface areas of 46 and 12 m<sup>2</sup>/g due

**Table 1**

Phase composition, specific surface area (SSA), total pore volume (PV), maximum pore diameter (PD), band gap energy ( $E_g$ ) and average crystallite size ( $D_{XRD}$ ) from XRD analysis, particle size D (W-width, L-length) from SEM and  $S_{BET}$  of synthesized anatase (A), brookite (B), rutile (R), and titania P25 (P25).

Sample	Composition (%)	SSA ( $m^2/g$ )	PV ( $cm^3/g$ )	PD (nm)	$E_g$ (eV)	Particle size (nm)		
						$D(S_{BET})$	$D(SEM)$	$D^3_{XRD}$
A	100	132	0.4908	10	3.25 <sup>1</sup>	11	10	10 <sup>a</sup>
B	100	116	0.1260	4	3.25 <sup>1</sup>	12	10	12 <sup>b</sup>
R	100	12	0.4480	89	3.34 <sup>2</sup>	117	W: 50–100L: 300–500	98 <sup>c</sup>
P25	80 (A), 20(R)	46	0.3186	36	3.29 <sup>1</sup>	31	25	21 <sup>a</sup> 67 <sup>c</sup>

<sup>1</sup> Indirect band gap.

<sup>2</sup> Direct band gap.

<sup>3</sup> Crystallite size determined from the width of (a) anatase {101}, (b) brookite {121}, and (c) rutile {110} reflection.

to their larger particle sizes of *ca.* 31 and 117 nm, respectively. The average particle size of titania polymorph calculated from the BET surface area and bulk density [87,88] agree with the particle sizes determined from XRD and SEM (Table 1).

The band gap energies ( $E_g$ ) of synthesized titania polymorphs were determined using the Tauc plots for both direct and indirect transitions (Fig. 6). The result shows a decrease in band gap energy in the order: amorphous titania > titania P25 > anatase ≈ brookite > rutile. The obtained band gap energy for direct transition is larger than the value for indirect transition. The band gap energies of anatase and brookite (3.25 eV) calculated for indirect transition are slightly larger than the value of 3.2 eV usually reported for the bulk TiO<sub>2</sub> and smaller than that of titania P25 (3.29 eV). These values compare well with those found in the literatures [62,63,89,90]. It indicates that all titania polymorphs can absorb light in the UV-vis region of sunlight (below 420 nm).

The structural and textural characterization data of synthesized titania polymorphs are summarized in Table 1. In summary, the XRD pattern and Raman spectroscopy confirm that all titania polymorphs are of high-purity and -crystallinity. Agglomerated spherical brookite and anatase particles have a small crystallite size of *ca.* 10 nm which is in good agreement with particle sizes obtained

by SEM and  $S_{BET}$ . Besides, rutile crystallizes in form of large rod-like crystals with size of *ca.* 500 nm. Brookite and anatase show high specific surface areas facilitating the adsorption of organic from aqueous solution. The obtained band gap energies of titania polymorphs show the light absorption in UV-vis region below 420 nm as required for the photocatalytic degradation of organic compounds in water under the sunlight.

### 3.3. The photocatalytic degradation

#### 3.3.1. Degradation of cinnamic acid (CA)

The photocatalytic activities of brookite (B), anatase (A), and rutile (R) were evaluated with different recalcitrant molecules and compared to that of titania P25 (Degussa). Firstly, the photocatalytic degradation of the more reactive cinnamic acid over synthesized titania polymorphs and titania P25 was studied (Fig. 7). The contribution of the adsorption to the abatement is low (1–2%). The result shows that cinnamic acid is quickly degraded with all photocatalysts. This is due to the reactive olefinic (−C=C−) bond [14] in the side chain of cinnamic acid molecules, which is easily attacked. With prolonged time, cinnamic acid is completely degraded and nearly mineralized in the treatment with both

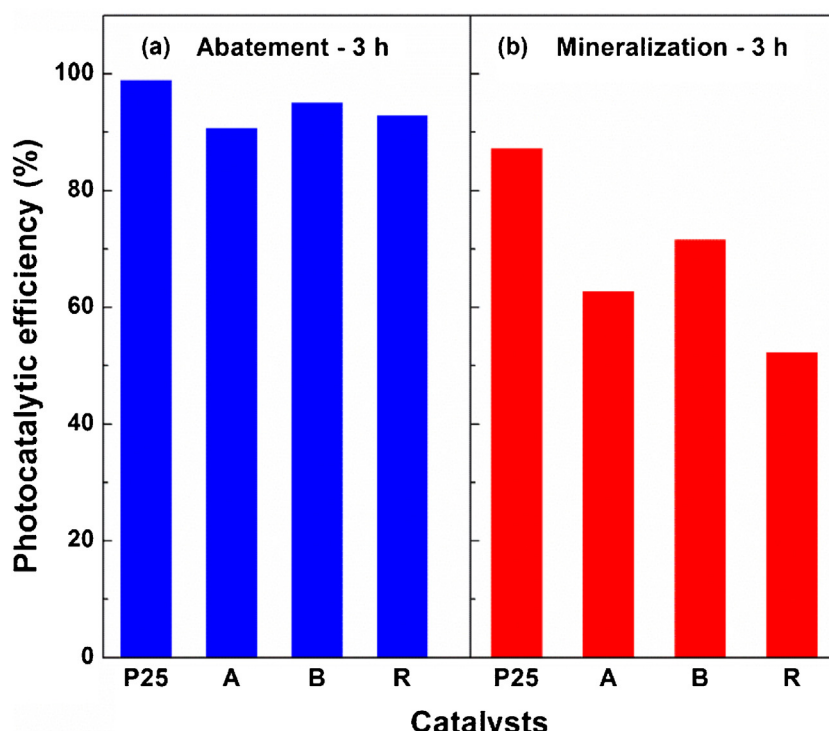


**Fig. 7.** Photocatalytic performance of anatase (A), brookite (B), rutile (R), titania P25 (P25) in the degradation of CA: abatement efficiency (a) and mineralization (b). Reaction conditions: RT, 10 ppm CA, 250 mL reaction solution, catalyst loading: 10 mg.

brookite and anatase. The lowest mineralization of CA was obtained with rutile showing the presence of a number of remaining intermediates or by-products which require longer time to decompose. After 3 h of reaction, already high abatement of cinnamic acid is observed with all titania photocatalysts and the differences in the photocatalytic activity are small. The differences are more pronounced in the mineralization of CA which decreases in the order: P25 > B > A > R.

### 3.3.2. Degradation of ibuprofen (IBP)

Next the photocatalytic degradation of the recalcitrant IBP was considered. The degradation of IBP during the course of photocatalytic treatment over the synthesized titania polymorphs brookite, anatase, rutile and for comparison titania P25 is shown in Fig. 8. The contribution of the adsorption in the dark (abatement at  $t = 0$ ) to the abatement of IBP is low. The adsorption capacity (mass percent) decrease in the order: A (1.27%) > P25 (1.08%) > B (0.61%) > R (0.45%). The BET surface areas of anatase and brookite are ca. 9–11 times higher than that of rutile (Table 1). The apparently similar adsorption capacity shows that the adsorption depends not only on the specific surface area or size of particles, but also on the shape of the crystals (facets). Obviously, the large planar facets of the rutile crystals facilitate the alignment of adsorbed molecules at the crystal surface leading to a markedly enhanced specific adsorption capacity per specific surface area. The degradation of IBP proceeds very fast at the onset of reaction (2 h). Ca. 97%, 86%, 82% of IBP are abated with titania P25, anatase, and brookite, respectively, (Fig. 8a). Nearly full degradation is achieved with these catalysts after 5 h of treatment. While the degradation of IBP with rutile proceeds much slower. Only ca. 80% of IBP is degraded with rutile after 5 h. Furthermore, the degradation of IBP with all the catalysts is accompanied by the formation of reaction intermediates/by-products as indicated by the appearance of a new absorption band at 262 nm [9,91], which disappears again with prolonged treatment (Fig. 8b). The formation of intermediates proceeds much slower with rutile indicating its lower photocatalytic activity.

The mineralization of IBP during the photocatalytic treatment was studied by TOC measurement and is shown in Fig. 8c. The different photocatalytic activity of the titania polymorphs is reflected in the mineralization performance: P25 (91%) > B ≈ A (84%) > R (28%) after 2 h of photocatalytic treatment. Compared to the rapid photocatalytic abatement detected by UV-vis spectra, the mineralization proceeds slowly. This is due to the fact that the UV-vis spectra are sensitive to the presence of aromatic ring, but do not detect non-aromatic degradation products and intermediates like organic acids. Therefore, the titania photocatalysts are very active in the aromatic ring opening of IBP which is nearly completed after 5 h of reaction. In contrast, the mineralization of IBP requires more time.

Electrospray ionization mass spectroscopy (ESI-TOF-MS) was used to study the formation of IBP intermediates during the photocatalytic treatment. Figs. 9 and 10a shows the negative ESI-TOF-MS spectrum of the starting 10 ppm IBP-Na salt aqueous solution. The  $[M-H]^-$  peak appears at  $m/z$  205 and is ascribed to the IBP anion [9,91,92]. Besides, lower and higher mass peaks appear at  $m/z$  89, 341, 501, 433, 661, and 889 indicating the presence of oligomeric or agglomerated IBP species are present in the starting solution. The ESI-TOF-MS spectra of IBP treated with anatase, brookite, rutile, and titania P25 after 1 h and 5 h are shown in Figs. 9 and 10, respectively. Compared to the spectrum of starting solution, the intensity of the IBP anion peak at  $m/z$  205 of the treated solutions is decreased markedly (ca. 5 times) in the treatment with both anatase and brookite at the onset of reaction (1 h). This mass peak disappeared completely after 5 h. With rutile, the intensities of the mass peaks of the starting solution decrease more slowly with photocatalytic treatment. Even after 5 h the mass peak of IBP is detected. Beside the decrease in intensity of IBP anion peak, the

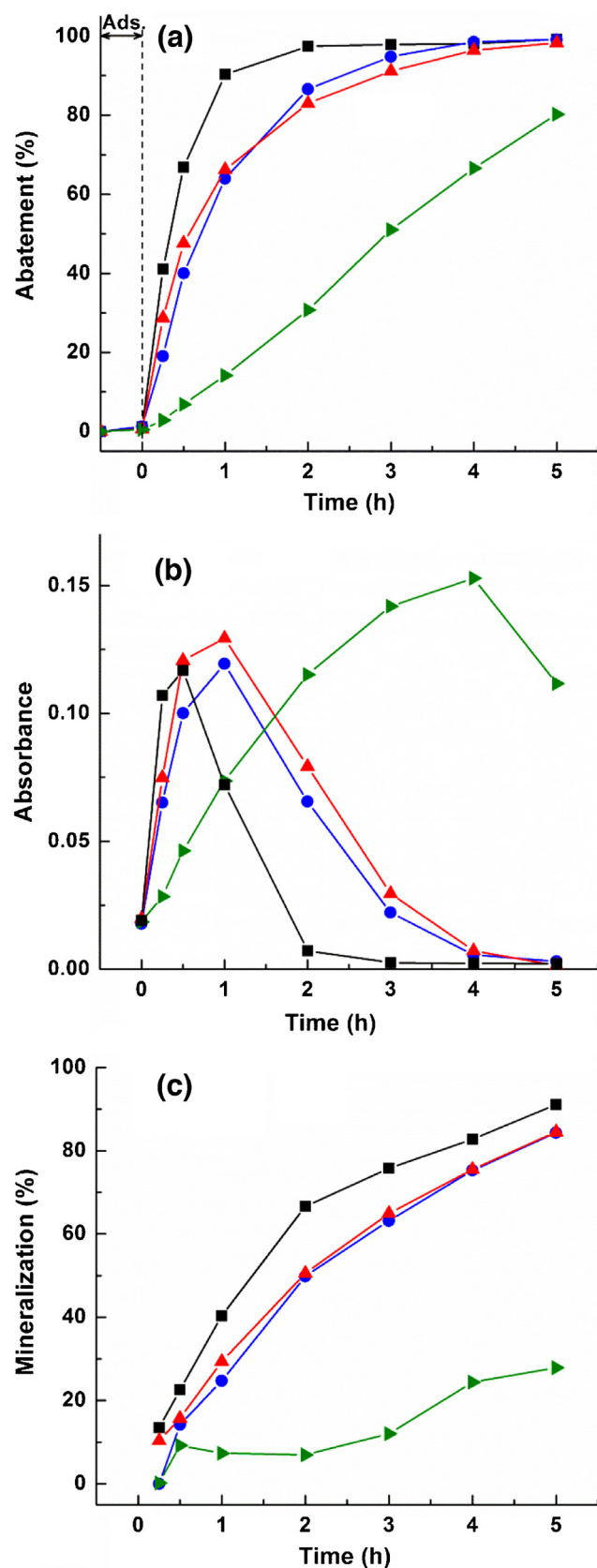


**Fig. 8.** Photocatalytic performance of titania catalysts in the degradation of IBP: (a) abatement of IBP, (b) formation of intermediates derived from UV-vis spectra, and (c) corresponding mineralization—(■) titania P25, (●) anatase, (▲) brookite, and (▲) rutile. Reaction conditions: RT, 10 ppm IBP, 250 mL reaction solution, catalyst loading: 10 mg.

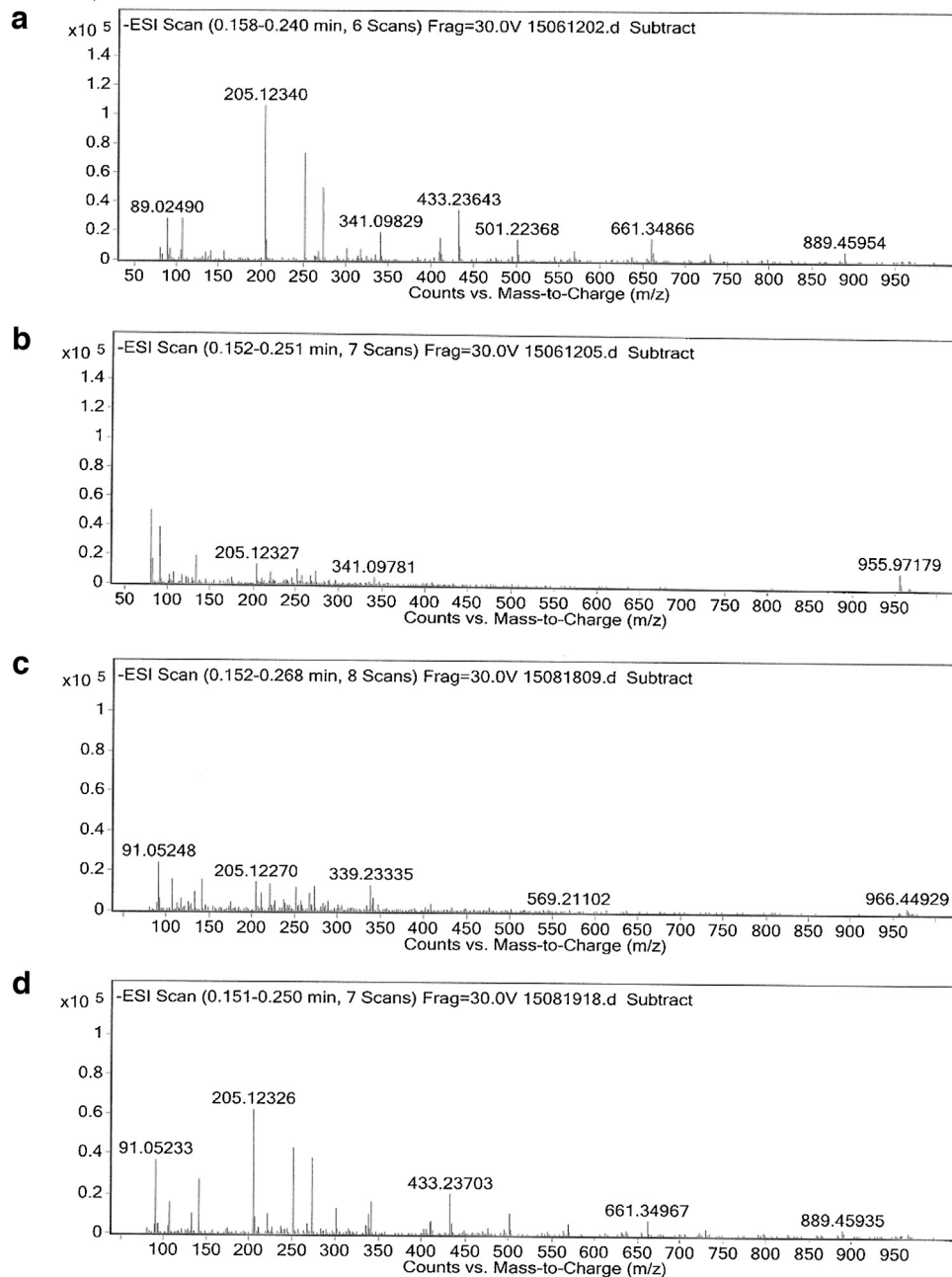


**Fig. 9.** Negative ESI-TOF-MS spectra of (a) 10 ppm starting IBP solution and IBP solution treated with (b) brookite, (c) anatase, and (d) rutile after 1 h. Reaction conditions: RT, 250 mL reaction solution, catalyst loading: 10 mg.

appearance of a couple of higher mass peaks is likely related to side chain and/or aromatic ring hydroxylation products. The intensities of these peaks decrease again with prolonged photocatalytic treatment. These results confirm the superior photocatalytic activity of brookite in the degradation of IBP, which compares to anatase.

### 3.3.3. Degradation of phenol (Ph)

In addition to ibuprofen and cinnamic acid, the photocatalytic degradation of phenol over titania P25, anatase, brookite, and rutile was studied (Fig. 11). The adsorption of Ph again has small impact on the photocatalytic abatement. In comparison to ibuprofen, the aromatic ring opening reaction proceeds slowly. Phenol behaves highly recalcitrant. The photocatalytic abatement of Ph increases linearly with prolonged irradiation time. Again the photocatalytic activity of brookite and anatase are similar, fol-

lowed by the lower active rutile. Only ca. 12% of Ph is degraded with rutile. The photocatalytic activity of titania polymorphs in the phenol degradation decreases in the following order: titania P25 > anatase ≈ brookite > rutile. The same behaviour is detected in the mineralization. Again anatase and brookite show the same degree of mineralization (ca. 45%).

The differences in the photocatalytic performance, the abatement of organics (aromatic ring opening) and mineralization, between synthesized titania polymorphs brookite, anatase, rutile, and commercial titania P25 are summarized in Tables 2 and 3:

The obtained abatement and mineralization show that in tendency the recalcitrance of organic compounds decreases in the order: Ph > IBP ≥ CA. The synthesized titania polymorphs anatase, brookite, and rutile show a general decrease in activity as follows: A ≈ B > R. Importantly, brookite is more active than anatase

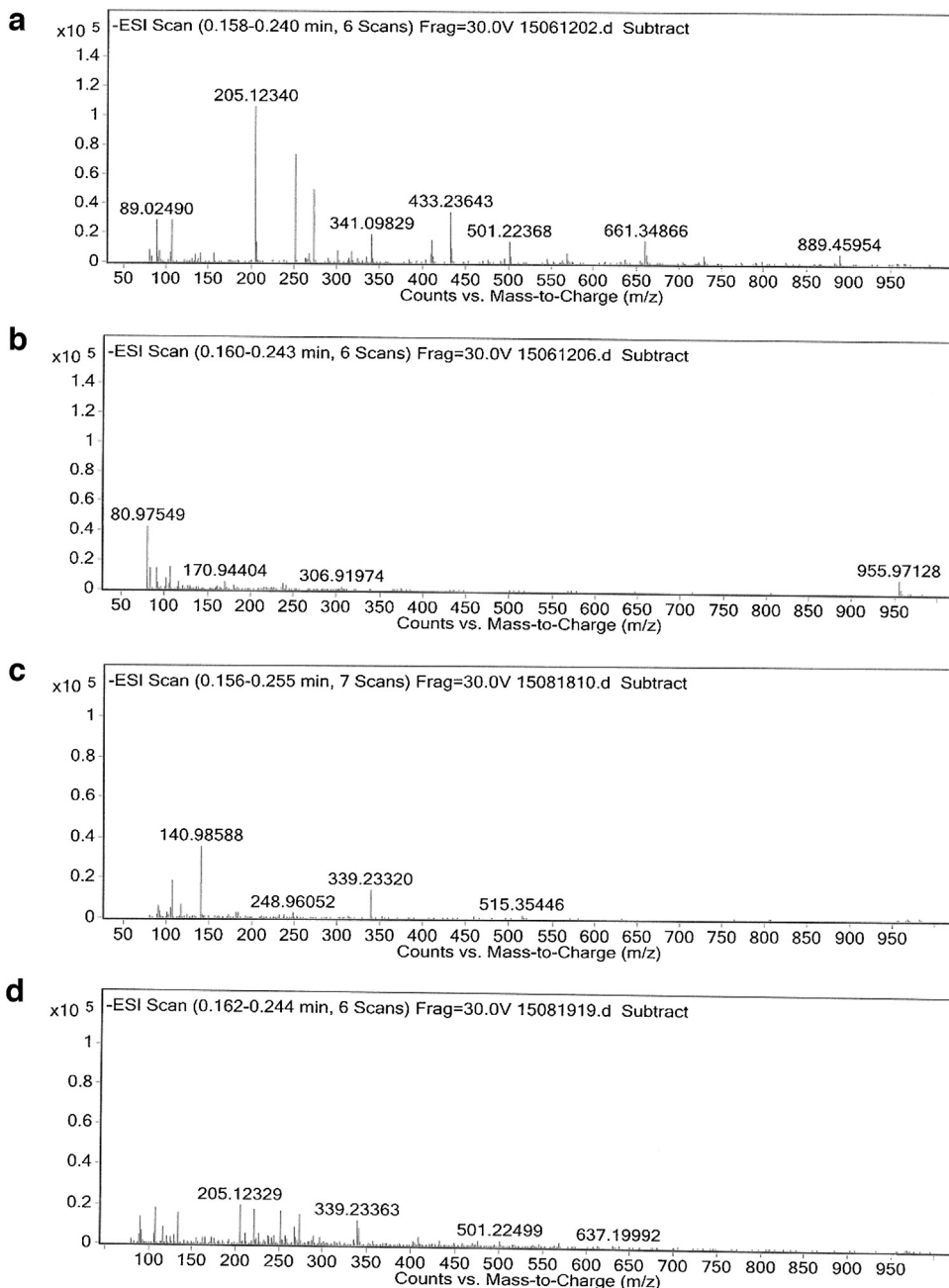


**Fig. 10.** Negative ESI-TOF-MS spectra of (a) 10 ppm starting IBP solution and IBP solution treated with (b) brookite, (c) anatase, and (d) rutile after 5 h. Reaction conditions: RT, 250 mL reaction solution, catalyst loading: 10 mg.

**Table 2**

The obtained abatement and mineralization of different organic compounds at the onset of photocatalytic degradation (2 h) treated with anatase (A), brookite (B), rutile (R), and titania P25 (P25).

Pollutants	Abatement (%)				Mineralization (%)			
	A	B	R	P25	A	B	R	P25
IBP	87	83	31	97	50	51	7	67
CA	76	88	94	95	36	52	38	63
Ph	23	31	3	55	13	15	3	35

in the onset of reaction (2 h), where the aromatic ring opening and hydroxylation of the phenyl group as well as side chain oxidation occur via oxidation by holes ( $\text{h}^+$ ) or hydroxyl ( $\cdot\text{OH}$ ) radicals [44]. Reported ring-opening products are mainly carboxylic acids and/or carboxylic acid derivatives [44,93,94], which are further

**Table 3**

The photocatalytic degradation of model organic compounds obtained after 5 h of photocatalytic treatment.

Catalyst	Abatement (%)	Mineralization (%)
Anatase	CA (99%) = IBP (99%) > Ph (57%)	CA (92%) > IBP (84%) > Ph (45%)
Brookite	CA (99%) ≈ IBP (98%) > Ph (54%)	CA (92%) > IBP (84%) > Ph (45%)
Rutile	CA (96%) > IBP (80%) > Ph (12%)	CA (69%) > IBP (28%) > Ph (8%)
Titania P25	CA (99%) ≈ IBP (99%) = Ph (99%)	CA (97%) > Ph (95%) > IBP (91%)

decarboxylated by the “photo-Kolbe” reaction to yield  $\text{CO}_2$  as final degradation product. Decarboxylation of propionic acid by holes is shown as an example [43] (Scheme 2).

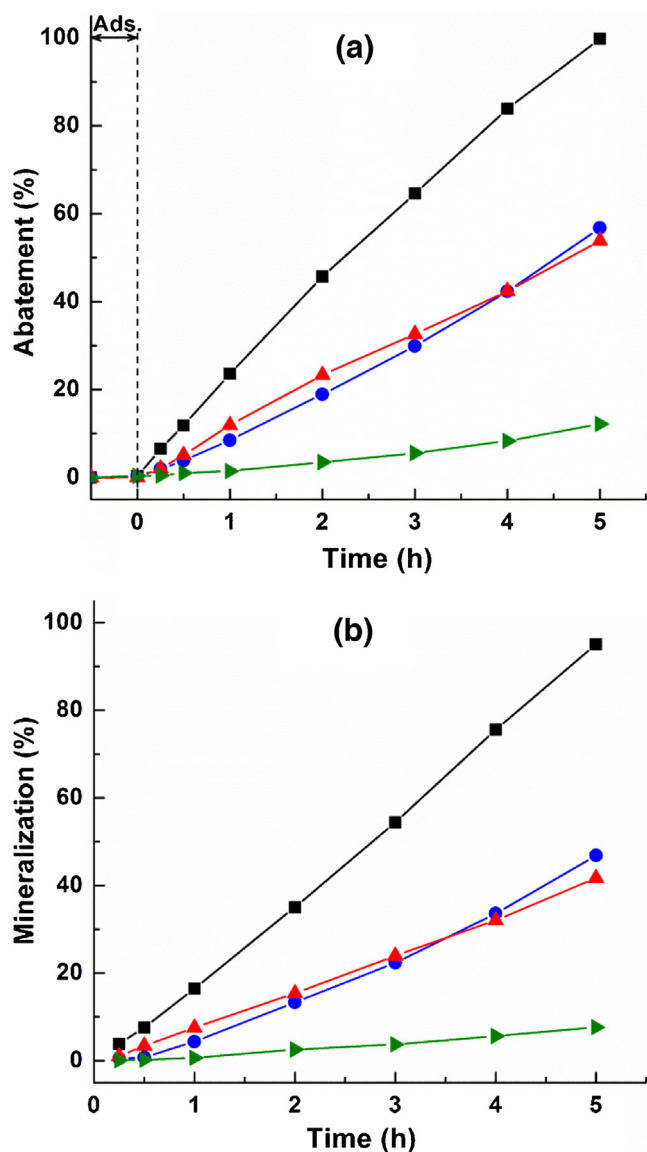
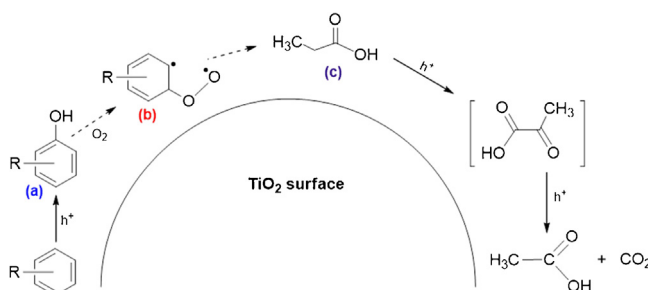


**Fig. 11.** (a) Abatement and (b) mineralization of phenol during the course of photocatalytic performance of (■) titania P25, (●) anatase, (▲) brookite, and (▶) rutile. Reaction conditions: RT, 10 ppm phenol, 250 mL reaction solution, catalyst loading: 10 mg.



**Scheme 2.** Proposed mechanism for the photocatalytic degradation of aromatic pollutants in water (a) hydroxylation, (b) aromatic ring opening, (c) decarboxylation.

#### 4. Conclusions

The titania polymorphs brookite, anatase, and rutile were obtained by hydrothermal synthesis using an amorphous titania as starting material under similar conditions in order to diminish the

impact of synthesis procedure on the photocatalytic properties of obtained brookite, anatase, and large crystal rutile. Different recalcitrant pollutants as cinnamic acid, ibuprofen and phenol were used to study the photocatalytic degradation behaviour. This approach allows achieving more reliable data on the differences between the three titania polymorphs. Brookite is a superior photocatalyst. It shows similar high activity as anatase. This finding is consistent with the similarity of both polymorphs regarding textural and optoelectronic properties as particle size, shape, specific surface area, and band gap. It confirms the importance of these properties for the photocatalytic performance. The general activity order is: P25 > A ≈ B > R. Remarkably, the activities of the hydrothermal synthesis brookite and anatase are close to that of titania P25, even they were obtained under much milder hydrothermal conditions (175–200 °C) compared to high temperature pyrolysis (>1800 °C) used with titania P25. This order is more pronounced in the mineralization behaviour. It proceeds more slowly due to the stepwise oxidative decarboxylation of the single carbon atoms of carboxylic acid intermediates.

#### Acknowledgments

This work has been supported by the European Union in the frame of the FP7 program (EU-project PCATDES). We are very grateful to Mrs. Petra Duncker for excellent assistant TOC analysis and Dr. Ung Thi Dieu Thuy for SEM analysis (Institute of Materials Science (IMS), Vietnam Academy of Science and Technology (VAST), Hanoi, Vietnam).

#### Appendix A. Supplementary data

Supplementary data associated with this article can be found, in the online version, at <http://dx.doi.org/10.1016/j.apcatb.2016.07.017>.

#### References

- [1] C. Gadipelly, A. Pérez-González, G.D. Yadav, I. Ortiz, R. Ibáñez, V.K. Rathod, K.V. Marathe, Ind. Eng. Chem. Res. 53 (2014) 11571–11592.
- [2] M. Carballa, F. Omil, J.M. Lema, M. Llompart, C. García-Jares, I. Rodríguez, M. Gómez, T. Ternes, Water Res. 38 (2004) 2918–2926.
- [3] T. Heberer, Toxicol. Lett. 131 (2002) 5–17.
- [4] S. Mompelat, B. Le Bot, O. Thomas, Environ. Int. 35 (2009) 803–814.
- [5] T.A. Ternes, Water Res. 32 (1998) 3245–3260.
- [6] S. Mompelat, O. Thomas, B. Le Bot, J. Environ. Monit. 13 (2011) 2929–2939.
- [7] E. Vulliet, C. Cren-Olivé, M.-F. Grenier-Loustalot, Environ. Chem. Lett. 9 (2011) 103–114.
- [8] F.S. Braz, M.R.A. Silva, F.S. Silva, S.J. Andrade, A.L. Fonseca, M.M. Kondo, J. Environ. Prot. 05 (2014) 620–626.
- [9] J. Choina, H. Kosslick, C. Fischer, G.-U. Flechsig, L. Frunza, A. Schulz, Appl. Catal. B: Environ. 129 (2013) 589–598.
- [10] J.C.C. Da Silva, J.A.R. Teodoro, R.J.C.F. Afonso, S.F. Aquino, R. Augusti, J. Mass Spectrom. 49 (2014) 145–153.
- [11] F.H. Li, K. Yao, W.Y. Lv, G.G. Liu, P. Chen, H.P. Huang, Y.P. Kang, Bull. Environ. Contam. Toxicol. 94 (2015) 479–483.
- [12] S. Roller, P. Seedher, Lett. Appl. Microbiol. 35 (2002) 350–394.
- [13] T. Fornari, R.P. Stateva, A. Berna, J. Chem. Eng. Data 54 (2009) 2263–2268.
- [14] F.S. Murakami, L.S. Bernardi, R.N. Pereira, B.R. Valente, Pharm. Chem. J. 43 (2009) 716–720.
- [15] P. De, M. Baltas, F. Bedos-Belval, Curr. Med. Chem. 18 (2011) 1672–1703.
- [16] D. Mantzavinos, Water Air Soil Poll. 3 (2003) 211–221.
- [17] C.M. Teh, A.R. Mohamed, J. Alloys Compd. 509 (2011) 1648–1660.
- [18] M.G. Alalm, A. Tawfik, Int. J. Chem. Mol. Nucl. Mater. Eng. 8 (2014) 144–147.
- [19] M. Choquette-Labbé, W. Shewa, J. Lalman, S. Shanmugam, Water 6 (2014) 1785–1806.
- [20] Z. Guo, R. Ma, G. Li, Chem. Eng. J. 119 (2006) 55–59.
- [21] E. Grabowska, J. Reszczynska, A. Zaleska, Water Res. 46 (2012) 5453–5471.
- [22] A.R. Rahmani, H. Rezaiehavidian, M. Almasi, A. Shabanlo, H. Almasi, Res. Chem. Intermed. (2016) 1441–1450.
- [23] S.J. Royae, M. Sohrabi, M. Jafarikour, Res. Chem. Intermed. (2015) 6409–6431.
- [24] A. Han, S. Chian, X. Toy, J. Sun, S. Jaenicke, G.K. Chuah, Res. Chem. Intermed. (2015) 9509–9520.

[25] J. Pal, M.K. Deb, D.K. Deshmukh, *Res. Chem. Intermed.* 41 (2015) 8363–8379.

[26] D. Kanakaraju, B.D. Glass, M. Oelgemöller, *Environ. Chem. Lett.* 12 (2014) 27–47.

[27] M.J. Gómez, M.J. Martínez Bueno, S. Lacorte, A.R. Fernández-Alba, A. Agüera, *Chemosphere* 66 (2007) 993–1002.

[28] V. Augugliaro, M. Bellardita, V. Loddo, G. Palmisano, L. Palmisano, S. Yurdakal, *J. Photochem. Photobiol. C: Photochem. Rev.* 13 (2012) 224–245.

[29] V. Augugliaro, M. Litter, L. Palmisano, J. Soria, *J. Photochem. Photobiol. C: Photochem. Rev.* 7 (2006) 127–144.

[30] A. Ibhodon, P. Fitzpatrick, *Catalysts* 3 (2013) 189–218.

[31] J. Herrmann, *Catal. Today* 53 (1999) 115–129.

[32] M. Litter, *Appl. Catal. B: Environ.* 23 (1999) 89–114.

[33] O. Tokode, R. Prabhu, L.A. Lawton, P.K.J. Robertson, *Environmental Photochemistry Part III*, in: D.W. Bahnemann, P.K. Robertson (Eds.), Springer, Berlin, Heidelberg, 2015, pp. 159–179.

[34] F. Méndez-Arriaga, M.I. Maldonado, J. Gimenez, S. Esplugas, S. Malato, *Catal. Today* 144 (2009) 112–116.

[35] H. Zangeneh, A. Zinatizadeh, M. Habibi, M. Akia, M. Hasnain Isa, *J. Ind. Eng. Chem.* 26 (2015) 1–36.

[36] R. Andreozzi, *Catal. Today* 53 (1999) 51–59.

[37] A.R. Ribeiro, O.C. Nunes, M.F.R. Pereira, A.M.T. Silva, *Environ. Int.* 75 (2015) 33–51.

[38] M.R. Hoffmann, S.T. Martin, W. Choi, D.W. Bahnemann, *Chem. Rev.* 95 (1995) 69–96.

[39] T. Hirakawa, K. Yawata, Y. Nosaka, *Appl. Catal. A: Gen.* 325 (2007) 105–111.

[40] C. Wang, H. Liu, Y. Qu, *J. Nanomater.* 2013 (2013) 1–14.

[41] M. Muruganandham, R.P.S. Suri, S. Jafari, M. Sillanpää, G.-J. Lee, J.J. Wu, M. Swaminathan, *Int. J. Photoenergy* 2014 (2014) 1–21.

[42] T.D. Bui, A. Kimura, S. Ikeda, M. Matsumura, *J. Am. Chem. Soc.* 132 (2010) 8453–8458.

[43] X. Pang, C. Chen, H. Ji, Y. Che, W. Ma, J. Zhao, *Molecules* 19 (2014) 16291–16311.

[44] X. Pang, W. Chang, C. Chen, H. Ji, W. Ma, J. Zhao, *J. Am. Chem. Soc.* 136 (2014) 8714–8721.

[45] T.K. Tseng, Y.S. Lin, Y.J. Chen, H. Chu, *Int. J. Mol. Sci.* 11 (2010) 2336–2361.

[46] W.-K. Jo, T.S. Natarajan, *Chem. Eng. J.* 281 (2015) 549–565.

[47] T. Ohno, T. Higo, H. Saito, S. Yuajin, Z. Jin, Y. Yang, T. Tsubota, *J. Mol. Catal. A: Chem.* 396 (2015) 261–267.

[48] R. Kaplan, B. Erjavec, A. Pintar, *Appl. Catal. A: Gen.* 489 (2015) 51–60.

[49] G.M.R. Vinu, *J. Indian Inst. Sci.* 90 (2010) 189–230.

[50] H. Zhang, J.F. Banfield, *Chem. Rev.* 114 (2014) 9613–9644.

[51] J. Zhang, P. Zhou, J. Liu, J. Yu, *Phys. Chem. Chem. Phys.* 16 (2014) 20382–20386.

[52] D. Beydoun, R. Amal, G. Low, S. McEvoy, *J. Nanopart. Res.* 1 (1999) 439–458.

[53] D.A.H. Hanaor, C.C. Sorrell, *J. Mater. Sci.* 46 (2011) 855–874.

[54] R.J. Tayade, P.K. Surolia, R.G. Kulkarni, R.V. Jasra, *Sci. Technol. Adv. Mater.* 8 (2007) 455–462.

[55] J. Zhang, Y. Nosaka, *J. Phys. Chem. C* 118 (2014) 10824–10832.

[56] R. Kaplan, B. Erjavec, G. Dražić, J. Grdadolnik, A. Pintar, *Appl. Catal. B: Environ.* 181 (2016) 465–474.

[57] Z. Li, S. Cong, Y. Xu, *ACS Catal.* 4 (2014) 3273–3280.

[58] T.A. Kandiel, L. Robben, A. Alkaim, D. Bahnemann, *Photochem. Photobiol. Sci.* 12 (2013) 602–609.

[59] T. Luttrell, S. Halpegamage, J. Tao, A. Kramer, E. Sutter, M. Batzill, *Sci. Rep.* 4 (2014) 4043.

[60] V. Etacheri, C. Di Valentin, J. Schneider, D. Bahnemann, S.C. Pillai, *J. Photochem. Photobiol. C: Photochem. Rev.* 25 (2015) 1–29.

[61] A. Di Paola, M. Bellardita, L. Palmisano, *Catalysts* 3 (2013) 36–73.

[62] W. Hu, L. Li, G. Li, C. Tang, L. Sun, *Cryst. Growth Des.* 9 (2009) 3676–3682.

[63] D. Reyes-Coronado, G. Rodríguez-Gattorno, M.E. Espinosa-Pesqueira, C. Cab, R. de Coss, G. Oskam, *Nanotechnology* 19 (2008) 145605–145615.

[64] V. Štengl, D. Králová, *Mater. Chem. Phys.* 129 (2011) 794–801.

[65] M. Inada, K. Iwamoto, N. Enomoto, J. Hojo, *J. Ceram. Soc. Jpn.* 119 (2011) 451–455.

[66] A. Di Paola, G. Cufalo, M. Addamo, M. Bellardita, R. Campostrini, M. Ischia, R. Ceccato, L. Palmisano, *Colloids Surf. A: Physicochem. Eng. Asp.* 317 (2008) 366–376.

[67] A. Pottier, C. Chanéac, E. Tronc, L. Mazerolles, J.-P. Jolivet, *J. Mater. Chem.* 11 (2001) 1116–1121.

[68] Y. Cao, X. Li, Z. Bian, A. Fuhr, D. Zhang, J. Zhu, *Appl. Catal. B* 180 (2016) 551–558.

[69] W. Xu, S. Zhu, Y. Liang, Z. Cui, X. Yang, A. Inoue, D. Pan, *Mater. Res. Bull.* 73 (2016) 290–295.

[70] S. Wang, H. Yu, S. Yuan, Y. Zhao, Z. Wang, J. Fang, M. Zhang, L. Shi, *Res. Chem. Intermed.* (2016) 3775–3788.

[71] X. Shen, B. Tian, J. Zhang, *Catal. Today* 201 (2013) 151–158.

[72] J.-G. Li, T. Ishigaki, X. Sun, *J. Phys. Chem. C* 111 (2007) 4969–4976.

[73] B.K. Mutuma, G.N. Shao, W.D. Kim, H.T. Kim, *J. Colloid Interface Sci.* 442 (2015) 1–7.

[74] T. Ozawa, M. Iwasaki, H. Tada, T. Akita, K. Tanaka, S. Ito, *J. Colloid Interface Sci.* 281 (2005) 510–513.

[75] A.V. Vinogradov, V.V. Vinogradov, P. Gouma, *J. Am. Ceram. Soc.* 97 (2014) 290–294.

[76] M.-H. Yang, P.-C. Chen, M.-C. Tsai, T.-T. Chen, I.-C. Chang, H.-T. Chiu, C.-Y. Lee, *CrystEngComm* 16 (2014) 441–447.

[77] S. Cassaignon, M. Koelsch, J.-P. Jolivet, *J. Mater. Sci.* 42 (2007) 6689–6695.

[78] Y. Liao, W. Que, Q. Jia, Y. He, J. Zhang, P. Zhong, *J. Mater. Chem.* 22 (2012) 7937.

[79] S. Mahshid, M. Askari, M.S. Ghamsari, *J. Mater. Process. Technol.* 189 (2007) 296–300.

[80] Y. Wang, L. Li, X. Huang, Q. Li, G. Li, *RSC Adv.* 5 (2015) 34302–34313.

[81] J. Zhang, S. Yan, L. Fu, F. Wang, M. Yuan, G. Luo, Q. Xu, X. Wang, C. Li, *Chin. J. Catal.* 32 (2011) 983–991.

[82] M. Zhao, H. Xu, H. Chen, S. Ouyang, N. Umezawa, D. Wang, J. Ye, *J. Mater. Chem. A* 3 (2015) 2331–2337.

[83] Y. Hu, H.-L. Tsai, C.-L. Huang, *J. Eur. Ceram. Soc.* 23 (2003) 691–696.

[84] W.F. Zhang, Y.L. He, M.S. Zhang, Z. Yin, Q. Chen, *J. Phys. D: Appl. Phys.* 33 (2000) 912–916.

[85] G.A. Tompsett, G.A. Bowmaker, R.P. Cooney, J.B. Metson, K.A. Rodgers, J.M. Seakins, *J. Raman Spectrosc.* 26 (1995) 57–62.

[86] J. Yang, S. Mei, J.M. Ferreira, P. Norby, S. Quaresmā, *J. Colloid Interface Sci.* 283 (2005) 102–106.

[87] K.J.A. Raj, B. Viswanathan, *Indian J. Chem.* 48A (2009) 1378–1382.

[88] L. Jiqiao, H. Baiyun, *Int. J. Refract. Met. Hard Mater.* 19 (2001) 89–99.

[89] M. Koelsch, S. Cassaignon, J. Guillemoles, J. Jolivet, *Thin Solid Films* 403–404 (2002) 312–319.

[90] N. Boonprakob, J. Tapad, P. Jansanthea, B. Inceesungvorn, International Conference on Chemical, Metallurgy and Material Science Engineering (CMMSE-2015), August 10–11, Pattaya, Thailand, 2015.

[91] J. Choina, C. Fischer, G.-U. Flechsig, H. Kosslick, V.A. Tuan, N.D. Tuyen, N.A. Tuyen, A. Schulz, *J. Photochem. Photobiol. A: Chem.* 274 (2014) 108–116.

[92] M. Marković, M. Jović, D. Stanković, V. Kovačević, G. Roglić, G. Gojić-Cvijović, D. Manojlović, *Sci. Total Environ.* 505 (2015) 1148–1155.

[93] B. Wen, Y. Li, C. Chen, W. Ma, J. Zhao, *Chem. Eur. J.* 16 (2010) 11859–11866.

[94] J. Yang, J. Dai, C. Chen, J. Zhao, *J. Photochem. Photobiol. A* 208 (2009) 66–77.